Quantum simulation / Simulation quantique

Josephson ladders as a model system for 1D quantum phase transitions

Une chaîne supraconductrice comme simulateur de transitions de phases quantiques en une dimension

Matthew T. Bell [a], Benoît Douçot [b], Michael E. Gershenson [c], Lev B. Ioffe [b,*], Aleksandra Petković [d]

[a] *Department of Electrical Engineering, University of Massachusetts Boston, Boston, MA 02125, USA*
[b] *LPTHE, Université Pierre-et-Marie-Curie, 75005 Paris, France*
[c] *Department of Physics and Astronomy, Rutgers University, Piscataway, NJ 08854, USA*
[d] *LPT, IRSAMC, Université Paul-Sabatier, 31062 Toulouse cedex 4, France*

A R T I C L E   I N F O

A B S T R A C T

We propose a novel platform for the study of quantum phase transitions in one dimension (1D QPT). The system consists of a specially designed chain of asymmetric SQUIDs; each SQUID contains several Josephson junctions with one junction shared between the nearest-neighbor SQUIDs. We develop the theoretical description of the low-energy part of the spectrum. In particular, we show that the system exhibits a quantum phase transition of Ising type. In the vicinity of the transition, the low-energy excitations of the system can be described by Majorana fermions. This allows us to compute the matrix elements of the physical perturbations in the low-energy sector. In the microwave experiments with this system, we explored the phase boundaries between the ordered and disordered phases and the critical behavior of the system's low-energy modes close to the transition. Due to the flexible chain design and control of the parameters of individual Josephson junctions, future experiments will be able to address the effects of non-integrability and disorder on the 1D QPT.

R É S U M É

Nous proposons une nouvelle plateforme pour l'étude des transitions de phase quantiques en une dimension. Le système consiste en une chaîne de boucles de SQUID asymétriques spécialement configurées : chaque SQUID contient plusieurs jonctions Josephson, dont une partagée avec le SQUID voisin. Des expériences sous micro-ondes électromagnétiques nous ont permis d'explorer les lignes de transition entre phase ordonnée et phase désordonnée, ainsi que le comportement critique des états excités de plus basse énergie au voisinage de cette transition. Grâce à la flexibilité de la configuration des SQUIDS et à la possibilité de contrôler individuellement les paramètres de chaque jonction Josephson, ce système

---

* Corresponding author.
E-mail address: ioffe@lpthe.jussieu.fr (L.B. Ioffe).

1. Introduction

The idea of quantum simulations emerged in the early 1980s out of the realization of the fundamental difficulty of emulating complex quantum system using classical computers. Over time, this idea has evolved into a sub-field of quantum computing [1]. Similar to the quantum computers, quantum simulators are based on the networks of quantum bits (qubits), but, in contrast to the fully-fledged quantum computers, quantum simulators do not employ discrete gate operations and error correction codes. The quantum simulators with tunable parameters are designed to emulate only certain types of Hamiltonians. However, it is possible to show that a very general Hamiltonian can be simulated by a seemingly restricted class of spin chains with XX and YY interactions [2,3]. One hopes that such simulators will facilitate designing novel quantum systems and exploring phenomena and regimes inaccessible in the past. Furthermore, quantum simulators enable the experimental study of quantum annealing in the context of adiabatic quantum computation. Modern quantum simulators are based on several platforms, which include cold atoms [4,5], cold ions [6], and superconducting qubits [7].

Our research focuses on designing artificial spin systems – tunable 1D Josephson arrays with controlled interactions – that emulate the quantum 1D models. The integrable model of a 1D Ising spin chain in the transverse magnetic field serves as a paradigm in the context of nonequilibrium thermodynamics and quantum critical phenomena [8,9]. Both the transverse field Ising and XY models, being relevant to a broad range of physical systems, played a crucial role in the understanding of quantum phase transitions [9]. These models have generated a formidable body of theoretical activity over the past fifty years. Recently, these models played a crucial role in the development of quantum annealing techniques and adiabatic quantum algorithms [10].

In the past, the experimental study of quantum spin dynamics in 1D has been largely limited to microscopic spins in condensed-matter systems. It has been demonstrated that such quasi-1D spin materials as $LiHoF_4$ and $CoNb_2O_6$ can be continuously tuned across the quantum phase transition (QPT) [11–13]. Though these works opened up new vistas in the studies of transverse field Ising model, the experimental realization of 1D quantum spin models in well-controllable and tunable systems remains a challenge. Indeed, as an experimental tool, the quasi-1D spin systems in solids are limited in several respects: (i) the inter-chain interactions are not negligibly weak, and, thus, these systems are inevitably quasi-1D, (ii) the exchange interactions between the nearest-neighbor spins cannot be varied, (iii) the exchange interactions are the same for all pair of spins, which does not allow for exploring the effect of disorder and phase boundaries without adding a significant amount of impurities, and (iv) the available experimental tool for these systems – scattering of neutrons – interacts only with a narrow class of excitations. Flexibility in the design of artificial spin systems, which are free from these limitations, facilitates bridging the gap between the theoretical study of ideal spin chains and the experimental investigation of bulk magnetic samples. In particular, this flexibility allows one to address an important issue of the effects of disorder on the statics and dynamics of transverse field spin models. Recently, the transverse-field Ising model was realized in the chain of artificial and fully-controllable spins – eight flux qubits with tunable spin – spin couplings [10]. We pursue a similar approach using specially designed one-dimensional Josephson ladders.

The paper is organized as follows. In Section 2, we introduce the Josephson ladder as a novel platform for the study of the 1D quantum phase transitions. The theory of these quantum systems is presented in Section 3. The microwave experiments on the characterization of the spectra of these novel quantum systems are described in Section 4. The outlook is provided in Section 5.

2. 1D Josephson ladders

The Josephson ladders designed for the study of the 1D QPT represent a 1D chain of coupled asymmetric SQUIDs (Fig. 1). The unit cell of the ladders is similar to that of the Josephson arrays developed as superinductors (the elements with the microwave impedance much greater than the resistance quantum h/e^2) [14]. Each unit cell contains a single smaller junction with the Josephson energy E_{JS} in one arm and three larger Josephson junctions with the Josephson energy E_{JL} in the other arm (Fig. 1a). The adjacent cells are coupled via one larger junction.

The ladders are characterized by the ratio of Josephson energies of the larger and smaller junctions, $r \equiv E_{JL}/E_{JS}$. For r greater than the critical value r_0, the Josephson energy of the ladder as a function of the phase φ across the ladder has only one minimum at $\varphi = 0$ regardless of the magnitude of the external magnetic field perpendicular to the ladder's plane. The value of r_0 depends on the ladder length and on the strength of quantum fluctuations (in the quasiclassical case, $r_0 = 5$ for an infinitely long ladder) – see Section 3. The regime $r > r_0$, where the ladder can be characterized by the Josephson inductance $L_J \propto (\frac{\mathrm{d}^2 E_J(\varphi)}{\mathrm{d}\varphi^2})^{-1}$ [15], was comprehensively studied in [14].

If $r < r_0$, the double-minima dependence $E_J(\varphi)$ is realized over a range of the magnetic flux $\Phi_C < \Phi < \Phi_0 - \Phi_C$ where $\Phi_C(r)$ is the critical flux, $\Phi_0 = \pi\hbar/e$ is the flux quantum. Figs. 1c, d show that at a fixed $r < r_0$, the spontaneous sym-
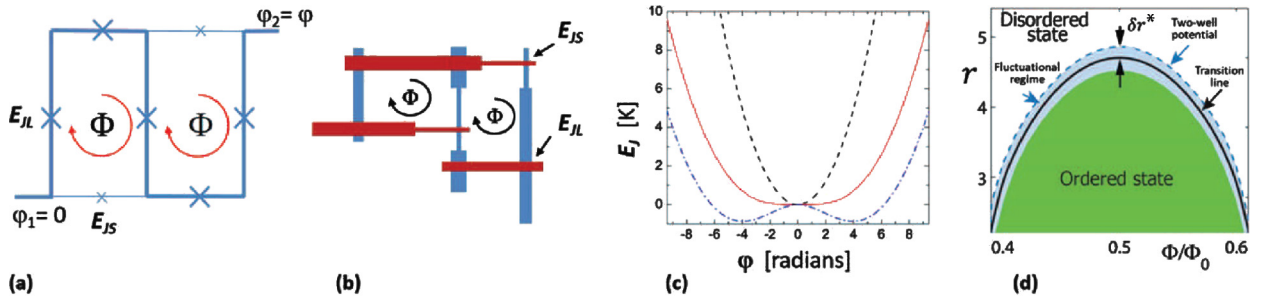
Fig. 1. The unit cells, potential energy, and the phase diagram of the Josephson ladder [14]. Panel (a): the unit cells of the ladder include smaller and larger Josephson junctions with Josephson energies E_{JS} and E_{JL}, respectively. All cells are threaded by the same magnetic flux Φ; the phase difference across the ladder is $\varphi_2 - \varphi_1 = \varphi$. Panel (b): the design of the ladder. Bottom electrodes of the Josephson tunnel junctions are shown in blue, top electrodes in red. Panel (c): the Josephson energy $E_J(\varphi)$ of a ladder with the ratio $E_{JL}/E_{JS} \equiv r < r_0$ calculated for three values of the flux: $\Phi = 0$ (dashed curve), $\Phi = \Phi_C$ (solid curve), and $\Phi = \Phi_0/2$ (dash-dotted curve). The energy is periodic in phase with the period 2π, here we show only a single branch. Panel (d): the phase diagram of the ladders on the r-plane. For $r < r_c(\Phi)$, the broken-symmetry phase is formed at $\Phi_C < \Phi < \Phi_0 - \Phi_C$ as a result of the phase transition of the Ising type. The boundary of this ordered-state region is shown as the solid black curve. The extension of the fluctuational regime is of the order of $\delta r \approx 0.1$ for realistic arrays.

metry breaking occurs at a critical value of the flux $\Phi_C(r)$ and the single-minimum energy $E_J(\varphi)$ is transformed into a double-minima function. The Josephson inductance diverges with Φ approaching $\Phi_C(r)$ (hence, the term "superinductance"); quantum phase fluctuations eliminate the divergency.

In the double-minima regime, the direction of currents in the ladder unit cells induced by an external magnetic field can be viewed as two states of the 1/2 pseudo-spins. As the potential barrier between these states increases, the quantum phase fluctuations decrease and the global broken-symmetry state emerges. The appearance of the double-well potential in a single cell does not imply a global phase transition in the whole system. The large-scale quantum fluctuations destroy the global order parameter if the barrier between two minima is too small. The global order parameter is formed at $r_c(\Phi) < r_0$ as a result of the phase transition of the Ising type ($r_c(\Phi)$ corresponds to the solid black curve in Fig. 1d). The extension of the fluctuational regime is of the order of $\delta r \approx 0.1$ for realistic arrays. Note that the magnetic field that drives the ladder across the QPT, $B < \Phi_0/A$, where A is the area of the unit cell, is very weak (~ 1 G in our experiments).

We emphasize that Josephson ladders with $E_{JL}/E_{CL} \gg 1$ have exponentially small probability of phase slip processes in which the phase across the ladder changes by $\sim 2\pi$. This implies that the static offset charges on individual islands have no effect on the quantum states of the ladder. We shall neglect the effects of these charges and phase slip processes in the following discussion. The estimate for the phase slip rate can be found in [14].

The low-energy physics of the ladders close to the QPT can be mapped on the φ^4 model, which is relevant to a wide range of physical phenomena, from quark confinement to ferromagnetism. Near the critical point, this model is equivalent to the integrable model of 1D Ising spin chain in the transverse magnetic field. Flexibility of the array design and tunability of the parameters of individual Josephson junctions offer several unique opportunities for exploration of the 1D quantum phase transitions. For example, this novel platform facilitates the study of effects of non-integrability and disorder on QPTs and the emergence of ergodic behavior in almost integrable quantum systems.

3. Theory of long Josephson ladders

### 3.1. Effective action of the low-energy modes of the long chains

As we show below, the long chain displays the phase transition that occurs as a function of the ratio $r = E_{JL}/E_{JS}$ at a fixed flux through a unit cell, or at a fixed r as a function of the flux through each unit cell. As usual in phase transitions, the critical properties are not sensitive to the parameter that drives the transition, so we focus on the transition driven by r below. Small modifications introduced by transition driven by magnetic field were discussed in [14]. The most important is the fact that, close to $r = r_0$, the effective distance from the critical line is a quadratic function of $\Phi - \Phi_0/2$.

We start by reviewing the properties of short chains in which one can neglect the phase variations between adjacent elements and its variation in time. Consider a small portion of the fully frustrated ladder shown in Fig. 2. The translational invariance implies that the solution is described by two phases across larger junctions: α at the "vertical" junctions and β at the "horizontal" ones. The energy per unit cell that contains two larger and one smaller junctions is given by

$$E(\alpha, \beta) = -E_{JL}(\cos\alpha + \cos\beta) - E_{JS}\cos(\pi - 2\alpha - \beta) \tag{1}$$

At $E_{JL} \gg E_{JS}$ the first term in Eq. (1) dominates and $E(\alpha, \beta)$ has a minimum at $(\alpha, \beta) = (0, 0)$. The expansion near this point gives

$$E^{(2)}(\alpha, \beta) = \frac{E_{JS}}{2} \begin{bmatrix} \alpha & \beta \end{bmatrix} \begin{bmatrix} r - 4 & -2 \\ -2 & r - 1 \end{bmatrix} \begin{bmatrix} \alpha \\ \beta \end{bmatrix} \tag{2}$$
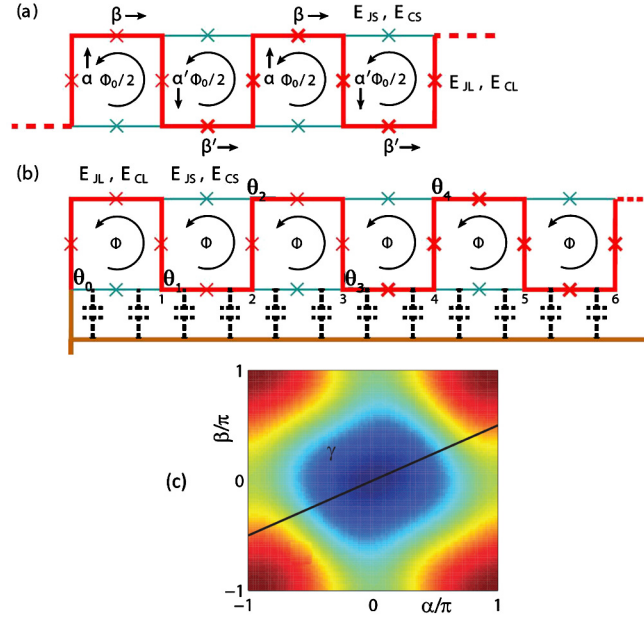
Fig. 2. Array schematics. Panel (a): exactly at full frustration, the classical ground state of the array corresponds to a translationally invariant pattern of phase differences $\alpha = \alpha'$, $\beta = \beta'$. Away from the full frustration, the period is doubled and phases $\alpha \neq \alpha'$, $\beta \neq \beta'$. In the absence of the ground capacitance, the kinetic energy of the array depends only on local phase differences α and β. For a generic fluctuation, the phases in different unit cells become different, $\alpha_j \neq \alpha$, etc. Panel (b): the presence of a non-zero ground capacitance leads to a small term that depends on the global phase $\Theta = \sum_{j<i}(\alpha_j + \beta_j)$ that becomes relevant for long chains. Panel (c) shows the energy as a function of the coordinates α, β. Close to the minimum the energy changes slowly in the direction indicated by the black line.

which is a quadratic form with eigenvalues E_{JL} and $(r-5)E_{JS}$. The second eigenvalue changes sign as the ratio $r = E_{JL}/E_{JS}$ decreases, signaling the instability and appearance of a nontrivial ground state. The long chains display the properties similar to the critical Ising model at r slightly less than the critical value of the ratio, $r_0 = 5$, as explained below.[1] Exactly at $r_0 = 5$, the function $E(\alpha, \beta)$ becomes flat along the eigenvector $(2,1)$, but remains steep in the orthogonal direction (see Fig. 2c). We introduce new coordinates in the "flat" and "steep" directions: $\gamma = (2\alpha + \beta)/\sqrt{5}$, $\delta = (\alpha - 2\beta)/\sqrt{5}$. Fig. 1c shows the energy plotted along the flat direction. Neglecting the phase deviations in the steep direction, the total phase across the unit cell is given by $\varphi_{eb} = 3/\sqrt{5}\gamma$.

At $r > r_0$, the ground state values of phases γ and φ, γ_0, and φ_0, are zero. Deviations of the total phase from $\varphi_0 = 0$ result in the quadratic increase of the energy

$$E^{(2)}(\varphi) = \frac{E_{JL}}{2} \delta r \, \gamma^2$$

where $\delta r = (r - r_0)/r$. At the optimal point ($\delta r = 0$), the phase stiffness vanishes and the phase fluctuations are limited by the next-order quartic term:

$$E^{(4)}(\gamma) = \frac{1}{24}\left(25 - \frac{17r}{25}\right)E_{JS}\gamma^4 \approx 0.9\,E_{JS}\gamma^4 \tag{3}$$

where in the last equality we replaced the numerical coefficient by its value at $r = r_0$. At smaller $r < r_0$, the ground state corresponds to a non-zero value of $|\gamma_0(r)| \propto \sqrt{\delta r}$. The appearance of a non-zero γ_0 implies a phase transition that breaks Z_2 symmetry $\gamma \to -\gamma$.

Close to the phase transition, the phase fluctuations become relevant. We derive the action of these fluctuations assuming that they are slow in space and time. We begin with spatial fluctuations. For a general space-varying phase, one gets

$$E = -E_{JL}\sum_i(\cos\alpha_{i-1/2} + \cos\alpha_{i+1/2} + \cos\beta_i)$$

$$- E_{JS}\sum_i \cos(\pi - \alpha_{i-1/2} - \alpha_{i+1/2} - \beta_i)$$

---

[1] Short-scale quantum fluctuations may renormalize the value of r_0 by shifting it down: $r_0 = 5 - \delta r_{sh}$. This effect is numerically small ($\delta r_{sh} \lesssim 0.1$) for the chains studied experimentally and qualitatively irrelevant, so we neglect it in the following discussion.

where we label the phases of each wire by the coordinates of their centers, so that the phases of horizontal wires have integer coordinates and the centers of the vertical ones have half-integer coordinates. Expanding in the phases $\alpha_i, \beta_i \ll 1$ and taking the Fourier transform, we get the quadratic part of the energy of the fluctuation with momentum k:

$$E^{(2)}(k) = \frac{E_{JS}}{2} \sum_k [\alpha_k, \beta_k] \begin{bmatrix} r + 2\xi_k & \xi_k \\ \xi_k & r - 1 \end{bmatrix} \begin{bmatrix} \alpha_{-k} \\ \beta_{-k} \end{bmatrix} \tag{4}$$

where $\xi_k = -2\cos(k/2)$. Expanding it for small k and leaving only the contribution of the slow mode $\alpha = 2/\sqrt{5}\,\gamma$ and $\beta = 1/\sqrt{5}\,\gamma$, we get for the energy per unit cell

$$E^{(2)}(k) = \frac{1}{2} E_{JL} \left[\frac{3}{5r}(\nabla\gamma)^2 + \delta r\,\gamma^2 \right] \tag{5}$$

The kinetic energy per unit cell is due to the capacitances of the larger and smaller junctions. We assume that $C_L = rC_S$ and express the result in the units of $E_{CL} = (2e)^2/C_L$:

$$
\begin{aligned}
T &= \frac{1}{2\,E_{CL}} \left[\left(\frac{d\alpha}{dt}\right)^2 + \left(\frac{d\beta}{dt}\right)^2 + \frac{1}{r}\left(\frac{d(2\alpha + \beta)}{dt}\right)^2 \right] \\
&= \frac{(r+5)}{2r\,E_{CL}} \left(\frac{d\gamma}{dt}\right)^2
\end{aligned}
\tag{6}
$$

Away from the critical point, the interaction between fluctuations can be neglected. In this regime, the spectrum of the slow fluctuations characterized by (5), (6) is given by the relativistic dependence

$$
\begin{aligned}
\omega^2 &= (ck)^2 + m^2 \\
c^2 &= \frac{3}{5(r+5)} E_{JL} E_{CL} \\
m^2 &= \frac{r\,\delta r}{5(r+5)} E_{JL} E_{CL}
\end{aligned}
\tag{7}
$$

Note that at all r, the velocity is relatively small because it is due to the Josephson energy of the smaller junctions and the charging energy of the larger ones, so that the wave dispersion is always small in the Josephson chain of this type. As the optimal point $\delta r = 0$ is approached, the gap in the spectrum closes and the fluctuations become more relevant. At large $E_{JL}/E_{CL} \gg 1$, the width of the fluctuational regime, δr^*, where the effects of the interaction (3) are relevant, is small. In the following discussion of this regime, we assume $r \approx r_0 = 5$, so that the full action becomes

$$
\begin{aligned}
S &= \int L\,dt\,dx \\
L &= \frac{1}{E_{CL}}\left(\frac{d\gamma}{dt}\right)^2 + \frac{E_{JL}}{2}\left[\frac{3}{25}(\nabla\gamma)^2 + \delta r\,\gamma^2 + \frac{9}{25}\gamma^4\right]
\end{aligned}
$$

Rescaling the variables

$$
\begin{aligned}
x &= \frac{\sqrt{3}}{5} s \\
t &= \sqrt{\frac{2}{E_{JL} E_{CL}}}\,\tau \\
\gamma &= \frac{5}{3\sqrt{2}}\,\eta
\end{aligned}
$$

we reduce it to a fully dimensionless form

$$S = \frac{1}{2g} \int \left\{ \left(\frac{d\eta}{d\tau}\right)^2 + (\nabla\eta)^2 + \delta r\eta^2 + \frac{1}{2}\eta^4 \right\} d\tau\,dx \tag{8}$$

where

$$g = \frac{3\sqrt{6}}{5} \sqrt{\frac{E_{CL}}{E_{JL}}} \tag{9}$$

We estimate the width of the fluctuational regime where the spectrum (7) is not valid by computing the fluctuational corrections to the action (8). The leading correction to the coefficient of η^4 term is

$$\frac{9\,g}{8\,\pi\,\delta r}$$

so that the width of the fluctuational regime $\delta r^* \approx g$.

3.2. Mapping to the Ising model

The transition to the ordered state breaks Z_2 symmetry and belongs to the same universality class as the Ising model. In the ordered state, the field η acquires average $\eta = \pm\eta_0$ where $\eta_0 = (-\delta r)^{1/2}$; in this regime the low-energy excitations are domain walls with the static energy

$$\epsilon_0 = \frac{1}{\sqrt{2}}\frac{1}{g}\delta r^{3/2}$$

Because the time needed to create and destroy a domain wall is $\tau = \delta r^{-1/2}$, the action corresponding to this process is $S \sim \delta r/g$, which again tells us that the width of the fluctuational regime is $\delta r^* \approx g$.

Outside of the fluctuational regime, the kinetic energy of the domain wall moving with velocity v is

$$\frac{v^2}{2\sqrt{2}\,g}\delta r^{3/2}$$

implying the mass $m = \delta r^{3/2}/\sqrt{2}\,g$. The Lorentz invariant equation compatible with these limits for the domain-wall energy spectrum is

$$\epsilon(k) = (m^2 + k^2)^{1/2}$$

In the ordered phase and inside the critical fluctuational regime, the model should be similar to the quantum Ising model

$$H = \mathscr{T}\sum_i \sigma_i^x + J\sum_i \sigma_i^z \sigma_i^z$$

where t and J are smooth functions of δr. Comparing the spectra of the domain wall in the Ising model and action (8) we see that

$$J \approx m/2$$
$$\mathscr{T} \approx \frac{1}{2ma^2}$$

in the ordered phase at $J \gg \mathscr{T}$ where a is the distance between the Ising spins. The distance a is set by the domain wall size $a^2 = 1/|\delta r|$.

The Ising model has transition to the ordered state at $J = \mathscr{T}$. By translating it into the parameters of the original model, we see that the transition happens at

$$\delta r_c = -c\,g$$

where $c \sim 1$.

Close to the transition into the ordered state, the excitations of the Ising model are Majorana fermions

$$c_p^\dagger(k) = (-1)^{\sum_{j<k} n_p(j)}\sigma_p^+(k)$$
$$n_p(j) = \left[\sigma_j^z(p) + 1\right]/2$$

Qualitatively, these excitations describe the domain walls in the Ising model that propagate with a constant velocity exactly at the transition, i.e. they have relativistic spectrum (Fig. 3). The fermionic nature of these excitations describes the exclusion principle of domain walls. Generally, away from the transition point, the spectrum of these excitations is the same as for free but massive one dimensional fermions:

$$\epsilon(k) = 2\sqrt{\mathscr{T}^2 + J^2 - 2\mathscr{T}J\cos(ka)} \tag{10}$$

We now discuss mapping of the matrix elements of the physical operators to the operators of the Ising model. The physical currents through the individual junctions are $J = E_{JL}\sin\alpha$, $J = E_{JL}\sin\beta$ and $J = -E_{JS}\sin(2\alpha + \beta)$. Thus, the current
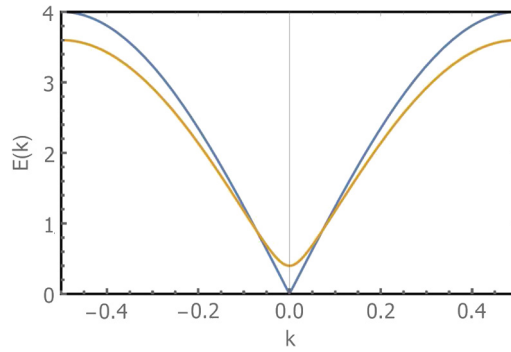
Fig. 3. Characteristic spectra of the excitations in the Ising model at and slightly away from the transition (blue and yellow curves, respectively). At low energies, the spectra become relativistic with the mass that vanishes at the transition. In the presence of a non-zero ground capacitance, the spectra as a function of k remain qualitatively similar.

operator is generally given by $J = c_J E_{JL} \eta$, where $c_J \sim 1$ is a numerical coefficient that depends on the particular current studied. In the critical regime in which locally $\eta = \pm \eta_0$, the current operator is directly related to the Ising variable

$$\hat{J}_{\text{eff}} = c_J E_{JL} \eta_0 \sigma^z \tag{11}$$

External flux noises interact directly with the current operators by $H_{\text{noise}} = \delta \Phi_{\text{ext}} \hat{J}$. Below we discuss the effect of this interaction on the decay and dephasing of Majorana modes with spectrum (10).

The charge operator associated with larger and smaller junctions are $Q_{L1} = i\, d/d\alpha$, $Q_{L2} = i\, d/d\beta$, $Q_S = i\, d/d(2\alpha + \beta)$. These charges interact with the potentials created by stray charges on each island. As before, we focus on the effect of this interaction with the soft modes described by the Ising variables. Consider a single unit cell described by the local Hamiltonian

$$H = -\frac{E_{CL}}{4} \left(\frac{d}{d\gamma} \right)^2 + \frac{1}{2} E_{JL} \left[+\delta r\, \gamma^2 + \frac{9}{25} \gamma^4 \right]$$

This Hamiltonian has two low-energy states $\Psi_{\pm}(\gamma)$ that correspond to symmetric and antisymmetric states that become eigenstates of Ising's operator σ_x after mapping to the Ising model. These states are split by the energy $\delta E = E_- - E_+$, which becomes $\delta E = 2t$ in the Ising model. Assuming that $\delta E \ll \sqrt{E_{CL} E_L}$, i.e. that the Ising modes are well separated from the rest of the spectrum, we can evaluate the matrix element of the charge operator $Q_\gamma = i\, d/d\gamma$ between these states:

$$\langle + | Q_\gamma | - \rangle = i \frac{\mathcal{T}}{E_c} \eta_0$$

The symmetry of the states guarantees that all other matrix elements of the charge are zero, thus

$$\hat{Q}_{\text{eff}} = \frac{\mathcal{T}}{E_c} \eta_0 \sigma^y \tag{12}$$

Note that the matrix element of the charge operator contains two factors that are small in the regime where the model (8) can be mapped to Ising's model: $\eta_0 \ll 1$ and $\mathcal{T}/E_c \ll 1$.

3.3. Matrix elements of the physical operators close to the critical point

Close to the critical point, the matrix elements of both the external charge and flux are given by operators that act on the effective Ising variables (11), (12). We evaluate the effect of these operators on the low-energy (Majorana) modes of the critical Ising model. To compute the matrix elements of the σ_i^y operator between the ground-state and low-energy excited states, it is convenient to use the Jordan–Wigner transformation in the form:

$$\sigma_i^x = 1 - 2 c_i^\dagger c_i \tag{13}$$

$$\sigma_i^z = \left(\prod_{j=1}^{i-1} (1 - 2 c_j^\dagger c_j) \right) (c_i + c_i^\dagger) \tag{14}$$

$$\sigma_i^y = \left(\prod_{j=1}^{i-1} (1 - 2 c_j^\dagger c_j) \right) i\, (c_i - c_i^\dagger) \tag{15}$$

Here it is assumed that we have a ladder with N unit cells, so the index i runs from 1 to N. Note that the Ising Hamiltonian is changed into its opposite after performing a π rotation around the x axis of the spins on one sublattice (e.g., for i even). Doing this changes the dispersion relation into:

$$\epsilon(k) = 2\sqrt{\mathscr{T}^2 + J^2 - 2\mathscr{T}J\cos(ka)} \tag{16}$$

which is convenient, because the minimum of this dispersion relation occurs at $k = 0$. Introducing $A_i = c_i + c_i^\dagger$ and $B_i = c_i^\dagger - c_i$ allows us then to write the Ising Hamiltonian as:

$$H = -\mathscr{T}\sum_{i=1}^{N} A_i B_i - J\sum_{i=1}^{N-1} B_i A_{i+1} \tag{17}$$

The single-excitation creation and annihilation operators $\gamma_k^\dagger$, γ_k are written as:

$$\gamma_k = \sum_{j=1}^{N}(\phi_j^k A_j + \chi_j^k B_j)$$

$$\gamma_k^\dagger = \sum_{j=1}^{N}(\phi_j^k A_j - \chi_j^k B_j) \tag{18}$$

where the coefficients ϕ_j^k and χ_j^k are real. These operators are determined by the condition that $[H, \gamma_k] = -\epsilon(k)\gamma_k$, which gives:

$$2t\phi_j^k - 2J\phi_{j+1}^k = -\epsilon(k)\chi_j^k \tag{19}$$
$$2t\chi_j^k - 2J\chi_{j-1}^k = -\epsilon(k)\phi_j^k \tag{20}$$

With the open boundary conditions, we have to solve these equations together with the constraints $\chi_0^k = 0$ and $\phi_{N+1}^k = 0$. The allowed values of k are determined by:

$$\frac{\sin(kaN)}{\sin(ka(N+1))} = \frac{\mathscr{T}}{J} \tag{21}$$

Note that $k = 0$ and $k = \pi$ are both excluded, because they lead to vanishing amplitudes ϕ_j^k and χ_j^k. Therefore, we have to search for real solutions in the interval $0 < k < \pi$. There are exactly N such solutions when $\mathscr{T}/J > \frac{N}{N+1}$, which corresponds to the paramagnetic phase. In the other case $\mathscr{T}/J < \frac{N}{N+1}$, we get only $N-1$ real solutions and one complex solution $k = i\kappa$, where κ is given by:

$$\frac{\sinh(kaN)}{\sinh(ka(N+1))} = \frac{\mathscr{T}}{J} \tag{22}$$

and the corresponding energy is:

$$\epsilon(i\kappa) = 2\sqrt{\mathscr{T}^2 + J^2 - 2\mathscr{T}J\cosh(\kappa a)} \tag{23}$$

which lies inside the gap of the infinite chain. The real solutions have the form:

$$\phi_j^k = \phi_0^k \frac{\sin(ka(N+1-j))}{\sin(ka(N+1))} \tag{24}$$

$$\chi_j^k = -\phi_0^k \frac{\epsilon(k)}{2J} \frac{\sin(kaj)}{\sin(ka)} \tag{25}$$

and the bound-state wave-function is obtained by analytical continuation from k to $i\kappa$. Canonical fermionic anticommutation relations are satisfied provided:

$$\sum_{j=1}^{N} \phi_j^k \phi_j^{k'} = \sum_{j=1}^{N} \chi_j^k \chi_j^{k'} = \frac{\delta_{kk'}}{4} \tag{26}$$

When $k = k'$, these relations fix the value of ϕ_0^k in the above expressions for ϕ_j^k and χ_j^k. Completeness can then be used to show that:

$$A_j = 2 \sum_k \phi_j^k (\gamma_k + \gamma_k^\dagger) \tag{27}$$

$$B_j = 2 \sum_k \chi_j^k (\gamma_k - \gamma_k^\dagger) \tag{28}$$

Note that the k sums have to incorporate the bound state when $\mathcal{T}/J < \frac{N}{N+1}$.

The ground state of the system $|0\rangle$ is determined by the condition that $\gamma_k |0\rangle = 0$ for all allowed k's. As shown earlier, we have to evaluate the matrix element of σ_i^y between the ground state and low lying states. The Jordan–Wigner representation for σ_i^y can also be written as:

$$\sigma_i^y = -i \left(\prod_{j=1}^{i-1} A_j B_j \right) B_i \tag{29}$$

so it is the product of an odd number of fermionic operators. Therefore, σ_i^y couples the ground state with the excited states containing an odd number of elementary fermionic excitations. The simplest of these states are of the form $\gamma_k^\dagger |0\rangle$. Evaluation of the matrix elements is straightforward, using Wick's theorem. For this, we need the basic correlators, which are easily determined from (27), (28), and the completeness relations:

$$\langle 0|A_i A_j|0\rangle = \delta_{ij} \tag{30}$$

$$\langle 0|B_i B_j|0\rangle = -\delta_{ij} \tag{31}$$

$$\langle 0|A_i B_j|0\rangle = -4 \sum_k \phi_i^k \chi_j^k \tag{32}$$

$$\langle 0|B_i \gamma_k^\dagger|0\rangle = 2\chi_j^k \tag{33}$$

Because the correlations of A_j operators with themselves are purely local, and similarly for the correlations of B_j operators, we see that upon computing $\langle 0|\sigma_i^y \gamma_k^\dagger|0\rangle$, each A_i has to be paired with a B_j, and $\gamma_k^\dagger$ has to be paired with the remaining B_j operator. This leads to the determinantal formula:

$$\langle 0|\sigma_i^y \gamma_k^\dagger|0\rangle = -i \, \mathrm{Det} C_i^k \tag{34}$$

Here, C_i^k is an $i \times i$ matrix given by:

$$C_i^k = \begin{pmatrix} G_{1,1} & G_{1,2} & G_{1,3} & \dots & G_{1,i} \\ G_{2,1} & G_{2,2} & G_{2,3} & \dots & G_{2,i} \\ \dots & \dots & \dots & \dots & \dots \\ G_{i-1,1} & G_{i-1,2} & G_{i-1,3} & \dots & G_{i-1,i} \\ D_1^k & D_2^k & D_3^k & \dots & D_i^k \end{pmatrix} \tag{35}$$

where $G_{i,j} = \langle 0|A_i B_j|0\rangle$ and $D_i^k = \langle 0|B_i \gamma_k^\dagger|0\rangle$, which are given by Eqs. (32) and (33), respectively. Such determinantal expressions for the Ising form factors are well known, see, e.g., [16]. For their actual evaluation on a finite-size chain with open boundary conditions, we used numerics. The results are shown in Fig. 4. As one might expect, the flux operator proportional to σ^z acquires large matrix elements in the ordered state. Because the ground state in a finite system is a symmetric combination of up and down ferromagnetically ordered states, the non-zero matrix elements correspond to the 01 transitions. Similarly, the charge operator acquires large matrix elements between the ground and the first excited states in the disordered state of the Ising model. In both cases, these matrix elements imply the decay rate of the first excited state. The matrix elements of the higher energy states display similar behavior.

3.4. Effect of a non-zero ground capacitance

In a realistic ladder of Josephson junctions, each element of the ladder has a non-zero ground capacitance, as shown schematically in Fig. 2b. For instance, in the ladders implemented experimentally, the ratio $C_G/C_L \approx 0.05$–0.1. Though small, such capacitance has significant effect on the low-energy spectrum because it introduces the terms in the effective action of the unit cell that depend on the time derivative of the total phase:

$$\delta L = \frac{1}{2 E_{CG}} \left(\frac{d\Theta}{dt} \right)^2 \tag{36}$$

where $E_{CG} = (2e)^2/C_G$ and the total phase Θ is related to the low-energy mode variable γ by $\nabla\Theta = 3/\sqrt{5}\,\gamma$.
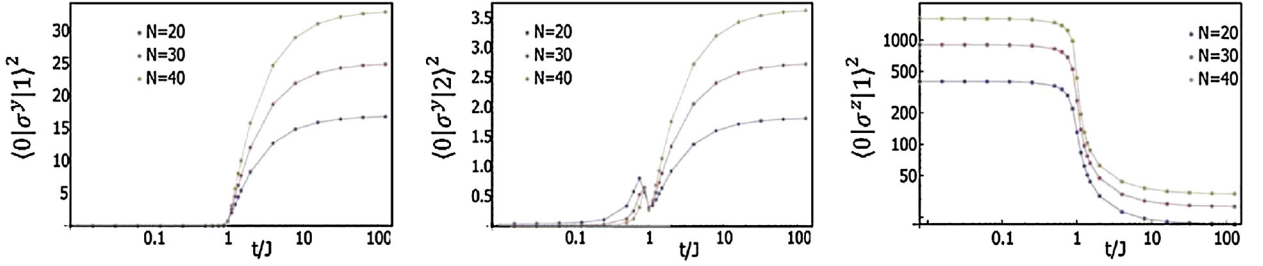
Fig. 4. Matrix elements of the relevant physical operators between the lowest energy states close to the quantum critical point of the Ising model; from left to right: the matrix element of the dimensionless charge operator σ^y between two lowest states, the same matrix element between the ground and the second excited state, and the matrix element of flux noise σ^z between the ground state and the lowest excited state.

The full kinetic energy of the low-energy modes becomes

$$T = \frac{(r+5)}{2 r E_{CL}} \left[1 + \frac{\kappa^2}{k^2} \right] \left(\frac{d\gamma}{dt} \right)^2 \tag{37}$$

where

$$\kappa^2 = \frac{9r}{5(r+5)} \frac{E_{CL}}{E_{CG}} \ll 1 \tag{38}$$

is the inverse characteristic length associated with the ground capacitance.

The appearance of the length κ^{-1} (38) implies that the effective Coulomb interaction between the charges is screened at distances $L > \kappa^{-1}$, in terms of the charge variable, q_γ conjugated to γ, the energy (37) becomes

$$T = \frac{r E_{CL}}{2(r+5)} \frac{k^2}{k^2 + \kappa^2} q_\gamma^2 \tag{39}$$

In the linear regime where non-linear effects can be neglected, this addition changes the spectrum (7) to become

$$\omega^2 = \frac{(c k)^2 + m^2}{1 + \frac{\kappa^2}{k^2}} \tag{40}$$

that displays additional softening at low-wave vectors $c k \ll (c\kappa, m)$: $\omega \approx m\kappa^{-1} k$. The softening of the spectrum (40) is observable only if it occurs outside of the critical regime, i.e. at $\delta r > g$, which corresponds to $\kappa > g \approx (E_{CL}/E_{JL})^{1/2}$.

In order to evaluate the effect of the ground capacitance on the low-energy modes in the critical regime, we evaluate the effect of the additional kinetic energy (36) on the effective action of the Majorana quasiparticles. It is convenient to represent the action as due to the interaction with the scalar field ϕ:

$$\delta L = i \frac{d\eta}{dt} \phi + \frac{E_G}{2} \left[(\nabla\phi)^2 + \kappa^2 \phi^2 \right] \tag{41}$$

where $E_G = (2/5) E_{CG}$. The last term in (41) is due to the screening of the Coulomb interaction at short scales discussed above. By repeating the same arguments that led us to (12) for the charge operator, the additional terms in Lagrangian density (41) can be translated into

$$\delta H = \mathscr{T} \eta_0 \sigma_i^x \phi(x_i) + \frac{E_G}{2} \left[(\nabla\phi)^2 + \kappa^2 \phi^2 \right] \tag{42}$$

for the effective Ising model that describes the vicinity of the transition point.

In the fermionic representation, these terms imply weak residual interaction between fermionic densities $\sigma_i^x = 1 - 2 c_i^\dagger c_i$. This interaction leads to the self-energy correction, $\Sigma(k)$, to the fermionic Green function. The important property of the long-range interaction between spins or fermionic modes (18) is its dependence on the momentum k but not on ω. Physically, it is due to the instantaneous and long-range nature of Coulomb interaction. Such interaction leads to the self-energy corrections that depend on the momentum but not on the frequency and thus violate the Lorentz invariance of the low-energy spectra. Qualitatively, the effect of the Coulomb interaction is to attract the spin flips (fermion densities) at short scales. The appearance of the frequency-independent $\Sigma(k)$ implies that the minimum of the energy $\omega_k(r)$ occurs at different r for different k.

In the experiment discussed in Section 4, we study the spectrum dependence on the flux, not on r. This is equivalent to the motion in the horizontal direction in the phase diagram of Fig. 1d instead of the vertical one. The shift in r of the position of the minima implies that the corresponding parabolas at which $\omega_k(r, \Phi)$ has a minimum are shifted up for larger k, which translates into the downshift in the value of the flux at which $\omega_k(\Phi)$ has a minimum for constant r.
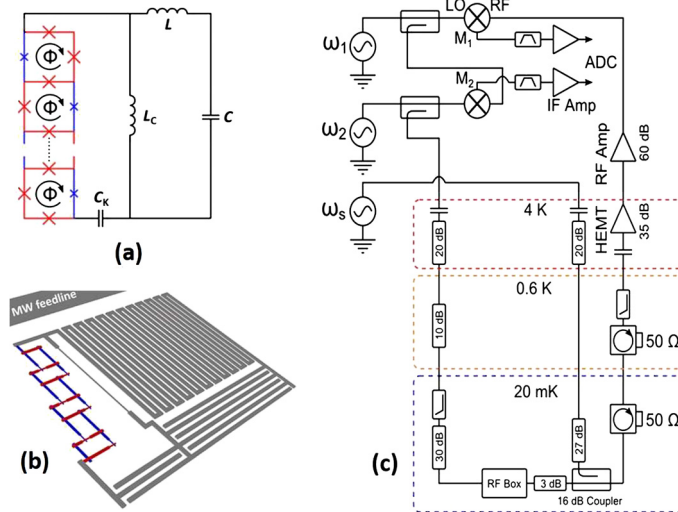
Fig. 5. Simplified diagram of the microwave setup [14]. Panel (a): schematic description of the on-chip circuit. The Josephson ladder, in combination with the capacitor C_K, forms a resonator that is coupled with the readout *LC* resonator via the kinetic inductance L_C of a narrow superconducting wire. Panel (b): the on-chip circuit layout of the tested circuit inductively coupled with the microwave (MW) feedline. Panel (c): simplified circuit diagram of the measurement setup.

The analytical expressions for the shift of $\omega_k(r, \Phi)$ can be obtained close to the Ising critical point. Exactly at the critical point of the Ising model without corrections (42), the fermionic density has power-law correlators, which translates into power-law correlations

$$\langle \sigma_0^x \sigma_r^x \rangle = \frac{1}{\pi^2 r^2}$$

which can be described as the correlator of the free bosonic fields, *s*. In this hydrodynamic description, the addition of the terms (42) does not change the quadratic nature of the energy. The Green function $D(\omega, k)$ of the Bose field acquires a self energy

$$\Sigma(k) = \frac{(\mathscr{T}\eta_0)^2}{E_G} \frac{1}{k^2 + \kappa^2}$$

that has no frequency dependence. This self energy correction has exactly the effect discussed above: it shifts the position of singularity in $D(\omega, k)$ away from the $\omega = \epsilon(k)$ line, which implies the shift in the spectrum of elementary (fermionic) excitations. In particular, the positions of the minima, $r_{\min}$, of $\omega_k(r, \Phi)$ as a function of r for different k occur at different r. The effect is maximal for $k \sim \kappa$ at which $\Sigma \sim cg$ that leads to the shift in $r_{\min} \sim g$.

4. Experimental data

Our microwave measurements were designed to explore the spectrum of the low-energy modes of Josephson ladders near the 1D QPT and the "lifetime" of these modes. The experimental set-up for these spectral and time-domain measurements has been described in Refs. [17,18]. Briefly, in these experiments, the Josephson ladder was coupled with the lumped-element readout resonator via the kinetic inductance L_C of a narrow superconducting film (Figs. 5a, b). The ladders, the readout circuits, and the microwave (MW) transmission line on the chip were fabricated using multi-angle electron-beam deposition of Al films through a lift-off mask (for fabrication details, see Refs. [14]). The in-plane dimensions of the Josephson junctions varied between 0.1×0.1 μm^2 and 0.3×0.3 μm^2; the area of a unit cell was 15 μm^2. The global magnetic field, which determines the fluxes in all superconducting loops, has been generated by a superconducting solenoid.

In the dispersive two-tone measurements of the ladder spectra, the resonance of the readout resonator was monitored at the probe frequency f_1, while the ladder was excited by the second-tone ("pump") frequency f_S (Fig. 5c). The microwaves were transmitted through the microstrip line coupled with the Josephson ladder and the *LC* resonator. The amplified signal was mixed by mixer M1 with the local oscillator signal at frequency f_2. The intermediate-frequency signal at $\Omega = f_1 - f_2 = 30$ MHz was digitized by a 1 GS/s digitizing card. The signal was digitally multiplied by $\sin(\Omega t)$ and $\cos(\Omega t)$, averaged over an integer number of periods, and its amplitude A and phase were extracted. The reference phase (which randomly changes when both f_1 and f_2 are varied in measurements) was found using similar processing of the low-noise signal provided by mixer M2 and digitized by the second channel of the ADC. Excitation of the modes resulted in a change of the ladder impedance [19]; this change was registered as a shift of the resonance of the readout resonator probed at f_1.
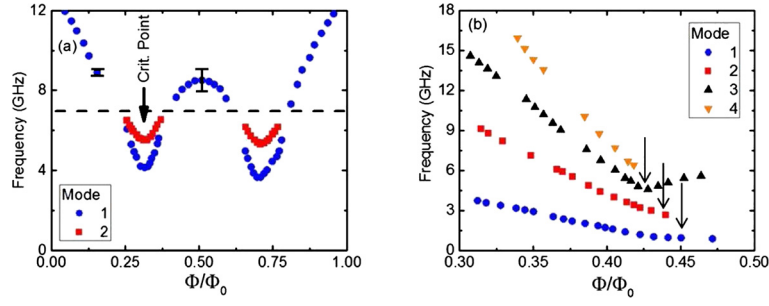
Fig. 6. Two-tone spectroscopy of the low-energy internal modes of the ladders with $r \leq r_0$ as a function of the magnetic flux in the unit cells. Panel (a): the data for a 24-cell ladder with $r = 3.2$. The resonance modes are periodic in the flux with the period Φ_0. Two critical points are located symmetrically with respect to $\Phi = \Phi_0/2$. At the critical points, the single-minimum dependence $E_J(\varphi)$ is transformed into a double-minima function; this corresponds to the QPT between the "paramagnetic" and "ferromagnetic" phases. Note the difference in the width of the resonances in the "paramagnetic" and "ferromagnetic" phases (shown as the error bars for two data points). Panel (b): the data for a 92-cell ladder with $r = 3.2$. The resonance frequencies of several low-energy modes are shown near the critical point. With approaching the critical point at $\Phi \approx 0.45\Phi_0$ we observed pronounced softening of the low-energy modes of the ladder. The resonances in the ferromagnetic phase are very broad (see the text), so the accuracy of finding the critical points is low. The minima positions can be extracted reliably from the remaining points by fitting with a polynomial curve. Arrows indicate the critical points, $\Phi_C(k)$, that are shifted for different modes due to the long-range interactions between the array's unit cells. In the limit of an infinitely long chain, we expect the critical point to be located at $\Phi = 0.46\,\Phi_0$.

The low-energy modes were measured as a function of the flux in the ladder's unit cells within the frequency range of our microwave setup 0.5–20 GHz.

In the time-domain experiments, we have observed Rabi oscillations for a "qubit" formed by the ladder and a shunting capacitance C_K. The ladder modes were excited by a short (~ 0.02–10 µs) MW pulse at the second-tone frequency f_S and the population of the excited level was recorded at the end of each pulse; the data were averaged over many repetitive measurements. The Rabi time for the lowest-energy mode exceeded 2 µs for the arrays with 92 unit cells. This observation demonstrates that the multi-junction arrays can be considered as quantum (not limited by decoherence) systems over a relatively long time scale. These measurements will be discussed elsewhere; below we focus on the spectroscopic data.

The results of measurements of the resonance frequencies for several low-energy modes of the ladder with $r < r_0$ are shown in Fig. 6. The nominal parameters[2] of the junctions in this chain were

$$E_{JS} = 4.8 \text{ K}, \ E_{CS} = 0.41 \text{ K}$$
$$E_{JL} = 15.6 \text{ K}, \ E_{CL} = 0.14 \text{ K} \tag{43}$$

For these parameters, we estimate $g \approx 0.1$. The ground capacitance in this experiment was $C_G \sim 0.05\,C_L$, so the characteristic length due to Coulomb interactions is $\kappa^{-1} \approx 5 \times (unit\,cell\,length)$. For these parameters one expects to observe the relativistic spectrum of the low-energy modes with $c \sim (10$–$20)\,[\text{GHz}] \times a_0$, where $a_0 \sim 3 \times (unit\,cell\,length)$; this would lead to the frequency difference between the lowest modes $\Delta f = 1$–$2\,\text{GHz}$, in good agreement with our observations. The frequency shift (defined as the difference between the minimal frequency of a mode and its frequency at $\Phi_C(0)$) due to the Coulomb interactions is approximately $\sim 0.3\,\Delta f$, which is compatible with the small value of $\kappa \approx 0.2 \times (unit\,cell\,length)^{-1}$.

The resonance frequencies depend on the flux periodically with the period $\Delta\Phi = \Phi_0$. We have observed the mode softening with approaching the quantum critical points, symmetrically positioned with respect to the flux $\Phi_0/2$. This is the key feature of the transverse-field Ising model. According to this model, the phases on both sides of the quantum critical point (the quantum paramagnet and ferromagnet, in the Ising spin terminology) are characterized by different types of excitations. In the paramagnetic phase, the relevant excitations are flips of individual spins. These excitations become gapless exactly at the critical point. In contrast, the excitations in the ordered (ferromagnetic) phase are the domain walls (or described as kinks) between different ground states ("vacua"). Even though any superconductor is a bosonic system, the lowest-energy excitations in the ladders are expected to have fermionic nature; the higher-energy excitations are composite particles made of these fermions (similar to the appearance of quarks and mesons). The emergence of non-trivial excitations near the quantum phase transition and their properties is one of the main themes of the present and future research.

The gradual shift of the minima of different modes shown in Fig. 6b is due to a non-zero ground capacitance of the unit cells that result in weak but non-negligible long-range interactions between the pseudo-spins in agreement with the theory presented in Section 3. The non-zero C_G is not a "bug" but a "feature": variation of the ground capacitance of individual cells enables fabrication of the devices characterized by different types of coupling between the unit cells, which makes possible the emulation of different quantum models such as Ising and XY models in transverse magnetic fields. Interactions

---

[2] The junction energies given below were computed by using the data for the junction area, measured resistance of the test junctions and Ambegaokar–Baratoff relation. This computation gives reliable values for E_{JL} and E_{CL}, but significantly overestimates the value of the Josephson energy for smaller junctions.
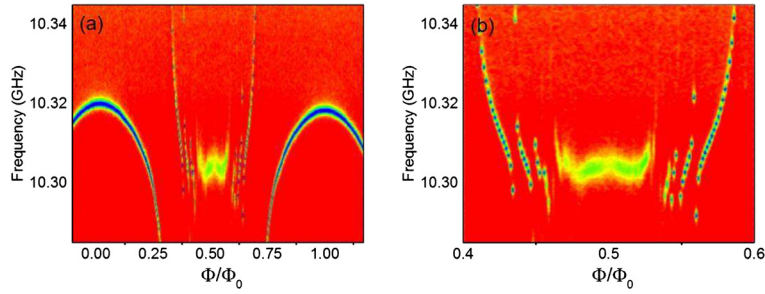
Fig. 7. The single-tone measurements for a long (92-unit-cell) chain [panel (b) is the blow-up of the data within the range [$0.4 < \Phi/\Phi_0 < 0.6$]. The avoided crossings between the low-energy modes and the readout resonator mode are clearly observed in the "paramagnetic" phase ($\Phi/\Phi_0 < 0.45$, $\Phi/\Phi_0 > 0.55$), where the readout resonance is sharp (the resonance width $\Delta f < 1$ MHz). In the "ferromagnetic" phase ($0.45 < \Phi/\Phi_0 < 0.55$), the resonance is smeared ($\Delta f \approx 4$ MHz) due to transitions between the low-energy modes induced by the flux noise (see the text for more details).

between the cells of Josephson arrays ("spins") can be tuned by changing the Josephson energies of the larger and smaller junctions. This tuning remains a challenge for other solid-state systems [8,9].

The accuracy of tracing the low-energy modes in the "ferromagnetic" phase is much lower than that in the "paramagnetic" phase (see Fig. 6b). Fig. 7 shows that in the single-tone measurements with a long 92-unit-cell chain, the readout resonance is dramatically broadened between the critical points. For this reason, in the two-tone measurements, we could not accurately determine the positions of low-energy modes for this chain in the ferromagnetic phase. We attribute this resonance "smearing" to a strong magnetic (flux) noise in our system. As shown in section 3.3, in the ordered (ferromagnetic) phase, the effect of the charge noise on the transitions between the low-energy states is weaker, whereas the effect of the flux noise is much stronger than that in the disordered (paramagnetic) phase. Note that the decay is proportional to the square of the matrix elements shown in Fig. 4, so the decay due to the flux noise is enhanced by a factor of $\sim 10^6$ in the ordered phase, while the decay due to the charge noise is reduced by a factor of $\sim 10^3$. The effect of the charge noise is further suppressed by a small factor that translates the matrix element of the Ising operators into the matrix element of the physical charge (the effect is opposite for the flux noise). By comparing equations (11), (12) relating the dimensionless matrix operators shown in Fig. 4 to the physical noise, we see that the decay rate due to the charge noise is additionally decreased by a factor $(t/E_c \eta_0)^2 \lesssim \delta r_c$, whereas the decay rate of the flux noise is enhanced by the factor $(E_{JL} \eta_0/\omega)^2$, where ω is the mode frequency. This makes the effect of the flux noise on the ordered side of the transition very large, whilst the effect of the charge noise remains moderate.

5. Conclusion and outlook

Controllable-by-design interactions between the pseudospins implemented as two states of the unit cells of periodic Josephson ladders enabled us to study the phase boundaries between the ordered and disordered phases and the critical behavior close to this transition. In particular, the study of microwave properties allowed us to characterize the low-energy spectrum of this system.

Close to the transition, the low-energy degrees of this system are described by the φ^4 model [9], which displays the transition between the ordered and disordered phases that belongs to the Ising universality class. In the Ising model, the low-energy excitations are Majorana quasiparticles, thus our observation of the low-energy modes of the long ladders can be viewed as a direct probe of Majorana excitations in this system. Note that, in contrast to the spin chains where only pairs of Majorana particles can be produced and studied by scattering techniques, Josephson ladders will allow us to study the full low-energy spectrum, in particular the fermionic excitations. An appealing analogy is provided by the particle physics in which fermionic excitations are quarks, while pair of those correspond to pions. In this analogy, the spectrum shown in Fig. 6 corresponds to quarks while the spectrum studied in spin chains – to pions.

The developed experimental platform can help to address various fundamental issues. First, disorder can be controllably introduced in this 1D system, and this enables the study of the appearance of intermediate glassy non-ergodic phases. Second, the platform allows for engineering interactions between pseudospins that violate exact integrability of the effective Ising model that describes the system at large scales. For instance, the ground state capacitance results in long-range attractions between kinks in the Ising model in the ordered state. This allows one to study how ergodic behavior reappears in almost integrable quantum systems.

We envision the future work that will address the emergence of the symmetries near the critical point in the Josephson ladders. By measuring microwave responses of the ladders in different phases and extracting the excitation spectra and their matrix elements, one can fully explore the behavior of this system near the critical point and extract the critical indices. By introducing controllable scattering in the junction parameters, one can explore the effects of disorder on the quantum phase transitions in 1D.

Another exciting line of research is the effect of non-integrability on the excitation decay and dephasing. Because, in the critical regime, the lowest energy excitations are equivalent to the ones of the effective Ising model at the critical point, the integrability implies that these excitations have an infinite lifetime. In realistic arrays, the integrability becomes approximate

and excitations acquire a finite, albeit long, lifetime. In the extensive time-domain measurements, the decoherence rate in the 1D Josephson ladders can be extracted from Rabi oscillations and Ramsey fringes as a function of proximity to the critical point. We expect that the residual interaction between quasiparticles leads to much faster decoherence rates at higher energy. These measurements address an important issue of the emergence of classicality in closed quantum systems.

A potential extension of these experiments is the intentional gradual variation of the unit cell parameters in the ladders. The idea is to produce ladders characterized by a smooth transition region between the states with broken and unbroken symmetry. The position of the phase boundary (or distance between two boundaries) within a ladder with gradual change in the position-dependent parameter $r(x)$ can be varied by the magnetic field that controls the proximity of individual cells to the critical point. We expect that the boundary between single-well ("paramagnetic") and double-well ("ferromagnetic") phases supports the zero-energy (Majorana) mode that can be probed by spectroscopic methods. A crucial question that we plan to address is the mechanisms of the decoherence relevant for this mode.

Finally, by combining few ladders together, one can get the experimental realization of very exotic quantum objects such as the two-channel Kondo problem with its $1/2 ln2$ entropy due to exactly degenerate Majorana quasiparticles [20].

Acknowledgements

References

[1] Nature physics, Nature physics insight – quantum simulation, 2012.
[2] G. De las Cuevas, T.S. Cubitt, Simple universal models capture all classical spin physics, Science 351 (6278) (2016) 1180–1183.
[3] T. Cubitt, A. Montanaro, S. Piddock, Universal quantum Hamiltonians, arXiv:1701.05182, 2017.
[4] I. Bloch, J. Dalibard, S. Nascimbène, Quantum simulations with ultracold quantum gases, Nat. Phys. 8 (2012) 267–276.
[5] A. Mazurenko, et al., A cold-atom Fermi–Hubard antiferromagnet, Nature 545 (2017) 462.
[6] R. Blatt, C.F. Roos, Quantum simulations with trapped ions, Nat. Phys. 8 (2012) 277.
[7] A.A. Houck, H.E. Tureci, J. Koch, On-chip quantum simulations with superconducting circuits, Nat. Phys. 8 (2012) 292.
[8] A. Dutta, G. Aeppli, B.K. Chakrabarti, U. Divakaran, T.F. Rosenbaum, D. Sen, Quantum Phase Transitions in Transverse Field Spin Models: From Statistical Physics to Quantum Information, Cambridge University Press, Cambridge, UK, 2015.
[9] S. Sachdev, Quantum Phase Transitions, Cambridge University Press, Cambridge, 1999.
[10] M.W. Johnson, M.H.S. Amin, S. Gildert, T. Lanting, F. Hamze, N. Dickson, R. Harris, A.J. Berkley, J. Johansson, P. Bunyk, E.M. Chapple, C. Enderud, J.P. Hilton, K. Karimi, E. Ladizinsky, N. Ladizinsky, T. Oh, I. Perminov, C. Rich, M.C. Thom, E. Tolkacheva, C.J.S. Truncik, S. Uchaikin, J. Wang, B. Wilson, G. Rose, Quantum annealing with manufactured spins, Nature 473 (2011) 195–198.
[11] D. Bitko, T.F. Rosenbaum, G. Aeppli, Quantum critical behavior for a model magnet, Phys. Rev. Lett. 77 (1996) 940–943.
[12] H.M. Ronnow, J. Jensen, R. Parthasarathy, G. Aeppli, T.F. Rosenbaum, D.F. McMorrow, C. Kraemer, Magnetic excitations near the quantum phase transition in the Ising ferromagnet, Phys. Rev. B 75 (2007) 054426.
[13] R. Coldea, D.A. Tennant, E.M. Wheeler, E. Wawrzynska, D. Prabhakaran, M. Telling, K. Habicht, P. Smeibidl, K. Kiefer, Quantum criticality in an Ising chain: experimental evidence for emergent E$_8$ symmetry, Science 327 (2010) 177–180.
[14] M.T. Bell, I.A. Sadovskyy, L.B. Ioffe, A.Yu. Kitaev, M.E. Gershenson, Quantum superinductor with tunable non-linearity, Phys. Rev. Lett. 109 (2012) 1–5, 137003.
[15] M. Tinkham, Introduction to Superconductivity, Dover Books, 2004.
[16] R.M. Konik, A. LeClair, G. Mussardo, Int. J. Mod. Phys. A 11 (1996) 2765.
[17] M.T. Bell, J. Paramanandam, L.B. Ioffe, M.E. Gershenson, Protected Josephson rhombus chains, Phys. Rev. Lett. 112 (2014) 167001.
[18] M.T. Bell, W. Zhang, L.B. Ioffe, M.E. Gershenson, Spectroscopic evidence of the Aharonov–Casher effect in a cooper pair box, Phys. Rev. Lett. 116 (2016) 107002.
[19] A. Wallraff, D.I. Schuster, A. Blais, L. Frunzio, J. Majer, M.H. Devoret, S.M. Girvin, R.J. Schoelkopf, Approaching unit visibility for control of a superconducting qubit with dispersive readout, Phys. Rev. Lett. 95 (6) (5 August 2005) 060501.
[20] M. Pino, A.M. Tsvelik, L.B. Ioffe, Unpaired Majorana modes in Josephson-junction arrays with gapless bulk excitations, Phys. Rev. Lett. 115 (2015) 197001.